ACS OMEGA

http://pubs.acs.org/journal/acsodf

Article

Exploring the Core Parameters of CNC-Based Chiral Nematic Structures for Enhancing the Dissymmetry Factor of Right-Handed Circularly Polarized Luminescence

Guodan Wei, Mengfan Lu, Kai Feng, Sijia Ma, Yuqian Jiang, and Zhaoxia Jin*

Cite This: *ACS Omega* 2023, 8, 23191−23201

Read Online

ACCESS | Metrics & More | Article Recommendations | Supporting Information

ABSTRACT: The chiral nematic nanostructure formed from cellulose nanocrystal (CNC) self-assembly has shown great potential as a matrix for generating circularly polarized luminescent (CPL) light with a high dissymmetry factor. Exploring the relationship between the device composition and structure and the light dissymmetry factor is crucial to a common strategy for a strongly dissymmetric CPL light. In this study, we have compared the single-layered and double-layered CNC-based CPL devices with different luminophores, such as rhodamine 6G (R6G), methylene blue (MB), crystal violet (CV), and silicon quantum dots (Si QDs). We demonstrated that forming a double-layered structure of CNCs nanocomposites is a simple but effective pathway for enhancing the CPL dissymmetry factor for CNC-based CPL materials containing different luminophores. The $|g_{lum}|$ values of double-layered CNC devices (dye@CNC5||CNC5) versus that of single-layered devices (dye@CNC5) are 3.25 times for Si QDs, 3.7 times for R6G, 3.1 times for MB, and 2.78 times for CV series. The different enhancement degrees of these CNC layers with a similar thickness may be due to the different pitch numbers in the chiral nematic liquid crystal layers whose photonic band gap (PBG) has been modified to match the emission wavelengths of dyes. Furthermore, the assembled CNC nanostructure has great tolerance to the addition of nanoparticles. Gold nanorods coated with the SiO_2 layer (Au NR@SiO_2) were added for enhancing the dissymmetry factor of MB in CNC composites (named MAS devices). When the strong longitudinal plasmonic band of the Au NR@SiO_2 matched the emission wavelength of MB and the PBG of assembled CNC structures simultaneously, the increase in the g_{lum} factor and quantum yield of MAS composites was obtained. The good compatibility of the assembled CNC nanostructures makes it a universal platform for developing strong CPL light sources with a high dissymmetry factor.

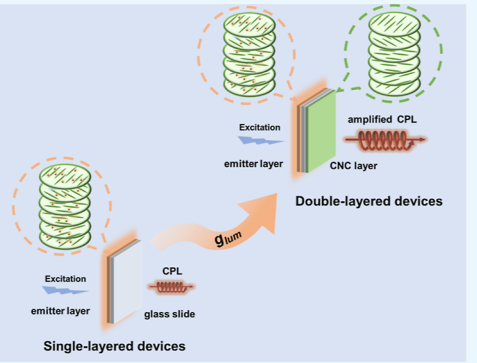

1. INTRODUCTION

Currently, the development of circularly polarized luminescent (CPL) materials is in the limelight of fundamental research and technological applications of optical data storage, sensors, and 3D displays.[1−3] The strong CPL light with a high dissymmetry factor has shown promising applications in enantioselective photopolymerization[4,5] and catalysis as well. However, the very low dissymmetry factor g_{lum} (10^{-3} to 10^{-4}) of common chiral luminophores[6] is far from the theoretical maximum and industrial requirement, thus limiting their applications.

Chiral fluorescent molecules or nanocomposites present an increased g_{lum} factor when they are in the chiral aggregate; thus, the construction of the chiral aggregate structure is an effective pathway for enhancing the dissymmetric factor of CPL systems.[7−9] The cholesteric liquid crystals (CLCs) are not only colored filters but also reflectors and polarizers.[10] CLCs as the chiral template possess incomparable advantages in acquiring high g_{lum} factors.[11] The chiral luminescent nanomaterials templated by the liquid crystal structure exhibit the enhanced CPL g_{lum} up to 10^{-1}.[11−13] Chen et al. reported that the g_e of a dye approached −2 in the 400−420 nm, while its emission wavelength was inside the resonance region of chiral nematic liquid crystals films at a thickness of 35 μm.[14] Moreover, the g_{lum} can be increased up to +1.51 in the composite containing chiral AIE-active donors, achiral AIE-active acceptors, and nematic liquid crystals, through leveraging the intermolecular energy transfer and chirality induction in the supramolecular assembled system.[15]

Not only these CLCs made by small molecules[16] and polymers[17] showed a distinct effect on enhancing the dissymmetric factor of circularly polarized luminescence but the cholesteric supermolecular structures composed of cellulose nanocrystals (CNCs)[1,18−20] have also presented effectiveness on boosting g_{lum}. CNCs are rod-shaped

Received: April 30, 2023
Accepted: May 9, 2023
Published: June 12, 2023

nanostructures obtained from the sulfuric acidic hydrolysis of natural cellulose sources such as wood, cotton, etc.[21,22] Driven by the entropically packing force of rod-shaped particles,[23] the CNCs in their aqueous solutions can self-organize into the CLC phase when their concentration is above a critical value. Afterward, the unique structure of evaporation-induced self-assembly (EISA) of CNCs can remain in the solid films, making them a promising matrix for functional materials.[24−28] Many investigations indicated that the chiral nematic liquid crystal structure of CNCs is a unique matrix for achieving high g_{lum} in composites.[29] Various achiral luminophores can emit chiral light after being co-assembled with CNCs.[1,30−35] However, the g_{lum} factor shows a big difference in literature, ranging from -10^{-2} to −0.46 for right-handed CPL[1,30−33] and +0.2−0.3 for left-handed CPL.[34,35] The determining factor of the g_{lum} in these composites has been explored tentatively so far. Liu et al. have observed that the overlap degree of the emission band of luminophores and the photonic crystal band gap (PBG) of CNCs modulated the g_{lum} values.[30,36] Tsukruk et al. also observed that the g_{lum} factor (−0.08) of CNC-PAA-Eu film can be increased to −0.46 by swelling the films using water spraying that makes a good match of the emission wavelength with the PBG of the CNCs assembled nanostructure.[32] On the other hand, Liu and coworkers have investigated several CPL systems, such as the UC($NaYF_4$/TmYb)-CNC[30] (g_{lum} factor −0.156 to −0.033), QD/CNC system[36] (−0.21 to −0.48), CNC/PVA/carbon dots composite with g_{lum} −0.27 and the large g_{RTP} factor up to −0.47.[31] The big change of g_{lum} factor in these CPL luminescent systems showed the luminophore-dependent property. Is there any optimum CNC-based device structure suitable for all fluorophores to improve their g_{lum}? What property of the fluorophores influences the g_{lum}? How to unleash the potential of CNC-based chiral nematic liquid crystal structures for a highly efficient CPL light source? Enhancing the g_{lum} in CNC-based CPL systems through a common strategy is a big challenge.

In this study, for elucidating the dominant properties of luminophores influencing the g_{lum}, we have compared the CPL dissymmetry factors of different CNC-based systems containing rhodamine 6G (R6G), methylene blue (MB), crystal violet (CV), and silicon quantum dots (Si QDs), respectively. To discover the impact of device structure on the g_{lum} factor, we compared the g_{lum} factor of devices with different structures, such as dye in the CNC layer (as R6G@CNCs single layer), dye in the PMMA layer and separated with a CNC layer (as R6G@PMMA||CNCs), and dye in the CNC layer and separated with another CNC layer (as R6G@CNCs||CNC double-layer). The comparison of R6G@CNC5 and R6G@PMMA||CNC5 confirmed that a separated CNC layer twisted the emission light stronger. Furthermore, the double-layer devices showed enhanced g_{lum} factors for all systems with different luminophores. In the double-layered devices, the increasing g_{lum} factor accompanied by the increase of pitch number of the separated CNCs films showed a limit at CNC7. The g_{lum} of the R6G@CNC5||CNC7 device at 575 nm showed a 4.2-times enhancement, from −0.25 (R6G@CNC5) to −1.05. Besides, gold nanorods coated with a thin SiO_2 layer (Au NR@SiO_2) were added to the MB@CNC5 layer (g_{lum} −0.15 at 675 nm) for enhancing the g_{lum}. When the strong longitudinal plasmonic band of the Au NRs matched the emission wavelength of MB and the PBG band of CNCs assembled nanostructures in the device simultaneously, the g_{lum} factor was enhanced to −0.608 at 675 nm. The simple double-layered device structure, and good compatibility make the assembled CNCs nanostructures a great platform for developing CPL light sources with a high dissymmetry factor.

2. EXPERIMENTAL SECTION

2.1. Materials. The ashless filter paper was supplied by Whatman Ltd. and used as the CNC source. Sulfuric acid (H_2SO_4, 98 wt %, analytical reagent) was purchased from Sinopharm Chemical Reagent Co., Ltd. Polyethylene glycol (PEG, M_w = 10k), poly(methyl methacrylate), rhodamine 6G (R6G, 95%, analytical reagent), and CV, (ACS reagent) were purchased from Shanghai Macklin Biochemical Co., Ltd. MB, (90%), 3-aminopropyltriethoxysilane (3-APTES), and tetramethoxysilane (TEOS, 98%) were purchased from Beijing J&K Scientific Co., Ltd. D-Glucose ($C_6H_{12}O_6{\cdot}H_2O$, analytical reagent), sodium borohydride ($NaBH_4$, ≥98.0%), and silver nitrate ($AgNO_3$, ≥99.8%, analytical reagent) were purchased from Tianjin Fuchen Chemical Reagent Technologies Co. Ltd. Tetrachloroauric(III) acid trihydrate ($HAuCl_4{\cdot}3H_2O$, 99.95 wt %, Au > 47.8%, ACS reagent) was purchased from Beijing Warwick Chemical Co., Ltd. Hexadecyltrimethylammonium bromide (CTAB, ≥97%) was purchased from Shanghai Accela ChemBio Co., Ltd. All reagents were used as received. Borosilicate glass slides (24 × 24 × 0.15 mm^3) were acquired from Citotest Labware Manufacturing Co., Ltd. The refractive index of borosilicate crown glass slides is ca. 1.52 (from the refractive index website).[37] All aqueous solutions were prepared by using deionized water (Millipore, 18.2 MΩ·cm).

2.2. Preparation of CNCs. CNC suspensions were prepared through the sulfuric acid-mediated hydrolysis of Whatman ashless filter paper according to our previous work.[38,39] Briefly, 5 g of filter paper was cut into small pieces and hydrolyzed in 50 mL of 64 wt % sulfuric acids at 45 °C under vigorous stirring for 45 min. Then, the resulting faint yellow slurry was added into cold deionized water (10-fold of the acid solution) to stop the hydrolysis. The resultant suspension was settled at room temperature for about 3 days. Afterward, the transparent top layer of the suspension was discarded and the cloudy residue was transferred into a dialysis bag (3500 molecular weight cutoff) and dialyzed against Millipore water at a low flow speed for 1 week until the pH of the water reached neutral. This final product was filtered through a 0.45 μm membrane and concentrated by evaporation at 40 °C to produce a CNC suspension with different concentrations (3, 4, 5, 6, 7, 8, and 9 wt %). The pH value of the final CNCs suspension was about 3−4.

2.3. Fabrication of Si QDs. Si QDs were synthesized according to literature.[4] One milliliter of 3-APTES solution was slowly added into 8 mL of D-glucose solution (0.1125 g/mL) under stirring. Subsequently, the mixed solution was stirred for 48 h at room temperature, and Si QD solution was obtained until the color of the solution changed from colorless to brown. The average size of Si QDs was 6.0 ± 1.6 nm. D-Glucose was used as a reductant during the synthesis. Finally, the Si QDs solution was dialyzed for 6 h and stored in the refrigerator at 4 °C for further use.

2.4. Fabrication of AuNR@SiO_2 Particles. Gold nanorods (Au NRs) were synthesized using a modified seed-mediated growth method.[40] In brief, a seed solution was prepared by mixing an aqueous solution of CTAB (9.75 mL, 0.1 M) with $HAuCl_4$ solution (0.25 mL, 0.01 M). Then, ice-cold $NaBH_4$ (0.6 mL, 0.01 M) was added. After stirring for 3 min, the seed solution was allowed to age for 2 h. Then, a

https://doi.org/10.1021/acsomega.3c02969
ACS Omega 2023, 8, 23191−23201

growth solution was prepared by mixing $AgNO_3$ (0.01 M), $HAuCl_4$ (8 mL, 0.01 M), ascorbic acid (0.88 mL, 0.1 M), and CTAB solution (80 mL, 0.1 M). The volume of $AgNO_3$ varied from 1, 1.28, 1.5, to 2 mL, for generating Au NRs with λ_{LSPR} of 630, 647, 667, and 730 nm, respectively. Gold nanorods (Au NRs) were obtained by adding 0.5 mL of the aged seed solution to the growth solution, followed by heating at 27 °C for 12 h. The resultant colloidal solution of gold nanorods was separated from the unreacted CTAB by 15 min centrifugation at 12,000 rpm, and the precipitate was redispersed in deionized water. The cleaning process was repeated twice and the obtained Au NR aqueous suspension was stored at 30 °C in a sealed glass bottle for further use. The Au NR solutions with the λ_{LSPR} of 630, 647, 667, and 730 nm showed a bluish, mazarine, amaranth, and reddish color, respectively.

To produce silica-coated gold nanorods, a certain volume of NaOH solution (0.1 M) was added to the above-prepared Au NR solution to acquire a pH > 10. Then, 60 μL of 20% (vol %) TEOS in ethanol solution was slowly added under stirring. After that, the mixture was stirred for 24 h for the silica coating. Finally, the mixture was centrifuged at 8000 rpm for 10 min. The acquired precipitate was washed twice with deionized water for removing unreacted chemicals. The λ_{LSPR} of gold nanorods was slightly red-shifted after coating with silica, to 635, 650, 670, and 735 nm, respectively.

To produce silica-coated gold nanorods, a certain volume of NaOH solution (0.1 M) was added to the above-prepared AuNR solution to acquire a pH > 10. Then, 60 μL of 20% (vol %) TEOS in ethanol solution was slowly added under stirring. After that, the mixture was stirred for 24 h for the silica coating. Finally, the mixture was centrifuged at 8000 rpm for 10 min. The acquired precipitate was washed twice with deionized water for removing unreacted chemicals. The λ_{LSPR} of gold nanorods was slightly red-shifted after coating with silica, to 635, 650, 670, and 735 nm, respectively.

2.5. Preparation of CNC-Based CPL Devices. *2.5.1. Luminophore@CNC5 Single-Layered Devices.* Five microliters of luminophores (Si QDs, R6G, CV, MB) aqueous solutions (1 mg/mL) were added into the CNCs suspensions (1 mL, 5 wt %). The mixtures were stirred for 90 min at room temperature. After that, the mixed suspensions were drop-casted by pipette on glass slides. The glass slide cast by the suspension was kept under an ethanol/water (60:40 v/v) atmosphere for 48 h to complete the EISA, and the luminophore@CNC5 single-layered devices were produced. To check the influence of film thickness in these single-layered devices, the CNC solution (1 mL) with different concentrations (3, 4, 5, 6, 7, 8, and 9 wt %) was used to generate R6G and MB series with different film thickness, which was denoted as R6G@CNC*x* or MB@CNC*x*, where *x* was 3−9.

2.5.2. Luminophore@PMMA||CNC5. Five microliters of luminophores (Si QDs, R6G, CV, MB) solution (1 mg/mL, dissolved in ethanol) was added into 1 mL of 5 wt % PMMA/dichloromethane solution. After stirring for 30 min, the homogeneous solution was drop-casted on a glass slide to form the dye@PMMA layer. Afterward, 1 mL of 5 wt % CNC suspension was cast on the back of the above glass slide to generate the pure CNCs layer. The glass slide was kept under an ethanol/water (60:40 v/v) atmosphere for 24 h to produce a dye@PMMA||CNC5 device.

2.5.3. Luminophore@CNC5||CNCx Double-Layered Devices. In brief, luminophore@CNC5 layers were obtained following Section 2.5.1, and then, 1 mL of CNC suspension with varied concentrations was drop-casted on the back of these glass slides. These glass slides were kept and dried under an ethanol/water (60:40 v/v) atmosphere for 2 days to conduct EISA, and luminophore@CNC5||CNC*x* double-layered devices were produced, where *x* = 3, 4, 5, 6, 7, 8, and 9 corresponding to the concentration of CNCs, 3, 4, 5, 6, 7, 8, and 9 wt %, respectively.

2.5.4. MAS@CNC5||CNCx Double-Layered Devices. Typically, 1 mL of 5 wt % CNCs suspension was mixed with 5 μL of MB solution (1 mg/mL). Then, 50 μL of AuNR@SiO_2 solution (1 mg/mL, λ_{LSPR} = 670 nm) was added into the CNCs/MB mixture. The mixed solution was stirred for 90 min at room temperature and drop-casted on the glass slide. The glass slide cast by mixed solution was dried under an ethanol/water (60:40 v/v) atmosphere for 48 h to obtain the MAS@CNC5 layer, which "MAS" represented MB mixed with AuNR@SiO_2. After that, 1 mL of CNC suspension with different concentrations was drop-casted on the back of the glass slide with the MAS@CNC5 layer to produce a pure CNC layer. Thus, MAS@CNC5||CNC*x* double-layered devices were produced, where *x* = 3, 4, 5, 6, and 7 corresponding to the concentration of CNCs 3, 4, 5, 6, and 7 wt %, respectively. The MAS@CNC5||CNC*x* double-layered devices loaded with AuNR@SiO_2 with different plasmon bands (λ_{LSPR} = 635, 650, or 735 nm) were also fabricated under the same conditions.

2.6. Characterizations of the Structure and Properties of CNC-Based CPL Devices. *2.6.1. Morphological Characterization.* Scanning electron microscopy (SEM, Hitachi SU8010) was conducted at an accelerating voltage of 3 kV to observe the cross-sectional morphology of the films. The fractured cross-sections of films were sputter-coated with a thin layer of gold before observation. Transmission electron microscopy (TEM, Hitachi H-7650) was operated at an acceleration voltage of 80 kV. The dilute samples were deposited on copper grids and dried in a vacuum oven at 25 °C overnight before TEM characterization.

2.6.2. UV−Vis, CD, and PL Spectroscopy. UV−vis absorption spectra were recorded from 300 to 1000 nm by using a Cary-60 spectrometer. Transmittance spectra were recorded, while the incident light angle was set at 90°, perpendicular to the films. PL spectra were recorded by using an FS5 fluorescence spectrometer (Edinburgh Instruments). The absolute quantum yields of the single-layered and double-layered devices were measured on Nanolog FL3-2iHR infrared fluorescence spectrometer (HORIBA Scientific). The circular dichroism (CD) spectra were recorded on a Chirascan spectrometer (Applied Photophysics) and the wavelength range was set from 300 to 1000 nm. The rotation measurements of the CD were measured on the JASCO J-1500 spectrometer.

2.6.3. CPL Measurement. CPL spectra were recorded on JASCO CPL-200 spectrophotometers, under the excitation light of 400 nm wavelength for R6G, MB, and CV systems, but 350 nm for the Si QD series. As for the R6G (aq)||CNC5 sample, 1 mL of R6G aqueous solution (5 μg/mL) was packed in a cuvette with a path length of 0.5 cm, and then, a pure CNC film formed by the self-assembly of 5 wt % CNCs suspension was placed between the cuvette and detector that ensures the emission light of R6G passed through the CNC film before it was detected.

2.6.4. GI-WAXS Measurement. GI-WAXS measurement was carried out at 1W1A Diffuse X-ray Scattering Station, Beijing

https://doi.org/10.1021/acsomega.3c02969
ACS Omega 2023, 8, 23191−23201

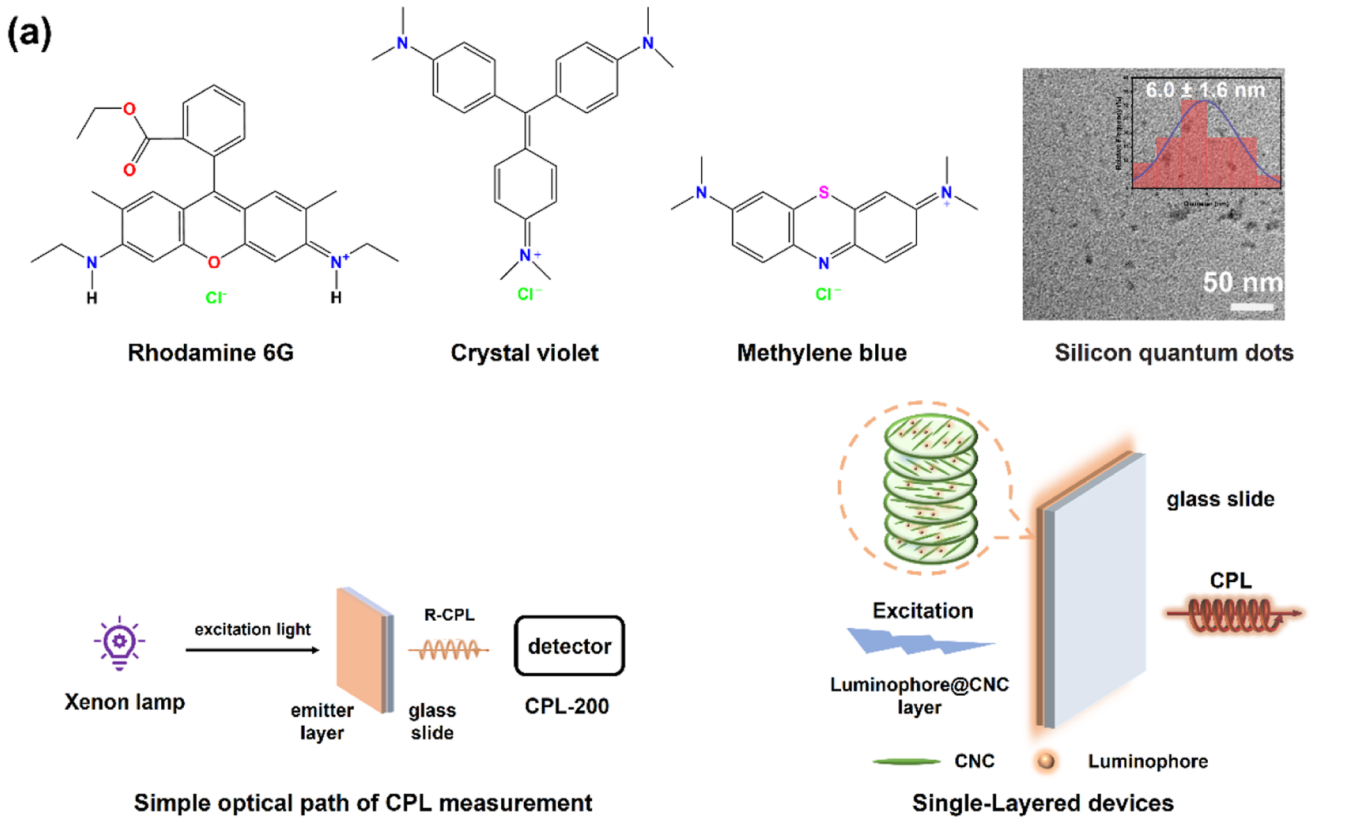

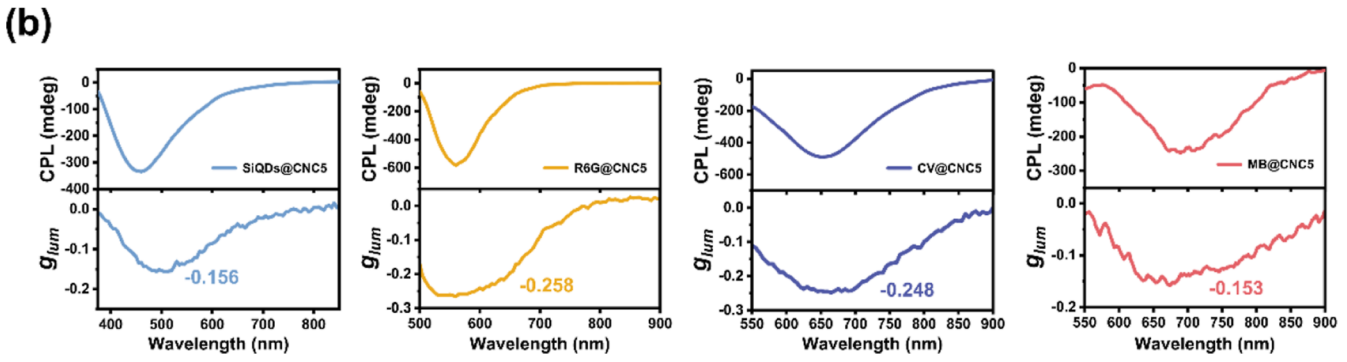

Figure 1. (a) Upper part: molecular structures of R6G, CV, and MB, respectively, and TEM image of Si QDs. The lower part: the illustrations of the optical path of CPL measurement and the structure of single-layered devices. (b) CPL spectra and g_{lum} factors of Si QDs, R6G, CV, and MB systems of single-layer devices. All film devices were fabricated by using 5 wt % CNC solution.

Synchrotron Radiation Facility (BSRF-1W1A). The wavelength of the radiation was 1.54 Å. The detector was Eiger, whose resolution was 1028 × 1062 pixels. The sample-to-detector distance was 113 mm and the incident light angle was set to 1°. The azimuthal intensity distribution curves were obtained using Fit2D software for the annular integral of the (1−10) crystal plane of the CNCs, with the azimuthal angle (φ) as the horizontal coordinate, and full-width at half-maximum (fwhm) calculated. Based on azimuthal intensity distribution curves, the degree of orientation (π) of CNCs was calculated according to eq 1

$$\pi = \frac{180 - \text{fwhm}}{180} \quad (1)$$

The degree of orientation (π) ranged from 0 to 1. $\pi = 1$ corresponded to a perfect orientation of the CNCs and $\pi = 0$ corresponded to a complete disorder of the CNCs.

3. RESULTS AND DISCUSSION

3.1. Comparison of the Single-Layer Devices of Four Systems. To investigate the impact of dyes composition on the CPL dissymmetric factor, several well-studied fluorophores, such as Si QDs, R6G, MB, and CV co-assembled with CNCs and formed a coating layer on the glass slide (Figure 1a). The reason for choosing them is the following: (1) the emission wavelengths of these fluorophores spanned the range of 500−700 nm, which is easily matched with the PBG band of CNCs self-assembled nanostructures. (2) They represented the different types of fluorophores, cationic type with good water solubility (R6G, CV, MB), and nanoparticle luminophore with good stability in aqueous dispersion (Si QDs). Because of the negative charge surface of CNCs particles, the cationic dye can be attracted to the CNCs surface under the electrostatic force. The comparison of these systems may help us find what kind of property features may modulate the g_{lum} in

https://doi.org/10.1021/acsomega.3c02969
ACS Omega 2023, 8, 23191−23201

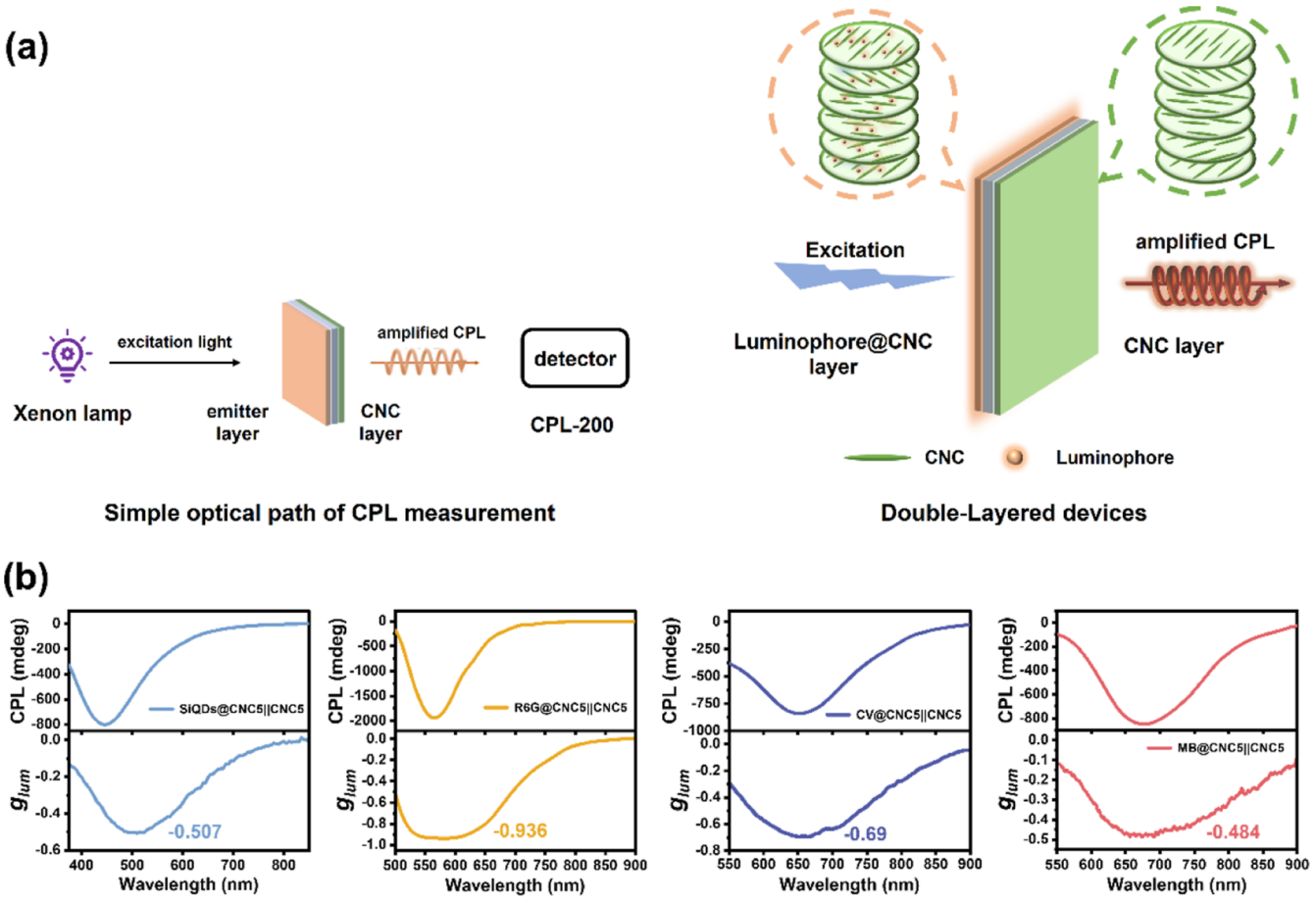

Figure 2. (a) Illustration of the measurement modes of the double-layered devices. (b) CPL spectra and g_{lum} factors of Si QDs, R6G, CV, and MB systems of double-layer devices. All these devices were fabricated using 5 wt % CNC suspension.

the CNC-based composites. These single-layer devices as luminophore@CNC5 were fabricated using 5 wt % CNCs solution. The PBG band of 5 wt % CNCs (575 nm) matched the emission band of R6G (570 nm); thus, the R6G@CNC5 was fabricated without additional treatment. For matching the CNC's PBG with the emission wavelength of Si QDs (~485 nm), NaCl was added to the Si QDs/CNC5 assembled system, and the PBG was blue-shifted to ~500 nm; for the CV and MB systems with emission wavelength at ~650 and 680 nm, the PEG (10 wt %, M_w 10k) was added in the CNC solution before assembly, and the obtained PBG bands located at ~655 or 675 nm, respectively. The transmission spectra, CD, and PL spectra of these films are presented in Figures S1 and S2, respectively. CPL light intensity and dissymmetric factors were measured by using CPL-200, under the excitation light of 400 nm wavelength for R6G, MB, and CV systems, but 350 nm for the Si QDs' case. The signal of the transmitted light was collected. The molecular structures of R6G, MB, and CV systems and TEM image of Si QDs are presented in Figure 1a, and CPL spectra and g_{lum} factors of these single-layer devices are shown in Figure 1b. These two cationic series, R6G@CNC5 and CV@CNC5, presented high g_{lum} values, −0.258 at 570 nm and −0.248 at 650 nm, respectively (Figure 1b). The circularly polarized luminescence systems based on R6G or its derivatives have been reported in the literature, with the $|g_{lum}|$ normally in the range of 10^{-2} to 10^{-3} after being dispersed in enantiomeric MOF crystals,[41] vortex field,[42] chiral dendritic films,[43] and electrospinning *R*(*S*)-PSA/PAN fibers.[44] Recently, Nam and Jeong demonstrated the highest $|g_{lum}|$ factor of 0.2−0.23 achieved by mixing R6G with the chiral plasmonic gold nanoparticles (R6G@Au).[45] The g_{lum} of the R6G@CNC5 single-layered device is comparable with this record. The MB@CNC5 single-layer device showed a g_{lum} factor of −0.153 at 677 nm, which is much higher than that reported in the literature, $|g_{lum}|$ 0.055−0.085 in the case of MB absorbed on Au@SiO_2 triangular nanoprisms and co-assembled with CNCs.[46] For the Si QD series, the g_{lum} was −0.156 at 490 nm, similar to that of the MB case, but it is lower than the literature report (−0.25).[4] R6G@CNCs single-layered devices with different thicknesses have been compared (Figure S3). The amount of R6G in these devices was kept the same. The $|g_{lum}|$ gradually increased from 0.237 to 0.292 in the concentration range from 3 to 9 wt %, respectively.

Besides, another single-layer device R6G@PMMA||CNC5 was fabricated and compared with the above-mentioned series. In this device, the fluorophore was dispersed in the PMMA layer and separated with the CNC layer (Figures S4 and S5). Surprisingly, it showed a g_{lum} factor of −0.74, much higher than the R6G@CNC device, and the g_{lum} of +0.20 was obtained by a reverse measurement (Figure S4a,b). If the CNC5 layer adhered on the measured cell of R6G aqueous solution, and let the emission light of R6G pass through the CNC layer before it got to the detector, the emission light was changed to right-handed as well, and the g_{lum} factor was −0.75 (Figure S4d). We thought that this R6G@PMMA||CNC5 single-layered device reflected the twisted strength of a pure CNC5 layer to the

https://doi.org/10.1021/acsomega.3c02969
ACS Omega 2023, 8, 23191−23201

emission light of R6G. If the concentration of the CNC layer was increased to 7 wt %, the g_{lum} can be further increased to −0.838 (Figure S4c). The value is comparable with the record-high g_{lum} factor of −0.87 reported by Xu and Zhang, in which a CNC layer was placed between the M1 (a fluorophore)-loaded PMMA layer and the CPL detector.[1]

Based on the above comparison of single-layer devices, we noticed that the existence of a CNC layer with a chiral nematic structure can twist the emission light of luminophores to a right-handed light with large dissymmetry. The significant difference in the g_{lum} factor of the two kinds of single-layered devices presented the influence of the device structure. When the fluorophores were dispersed in the CNC layer, irregular scattering effect in the CNC film may offset the twisting effect of the neat CNC-assembled nanostructure at a certain content.

3.2. Comparison of the Double-Layer Devices of Four Systems. For taking full advantage of the substrate-induced well-assembled CNC nanostructure, the double-layer device structure was fabricated on the front and back sides of the glass slides. On the back of these glass slides with the fluorophore@CNC5 layer, a pure CNCs assembled layer with different thicknesses was deposited by EISA of CNC solutions with varied concentrations. These devices were labeled as R6G@CNC5||CNC*x*, in which *x* presented the concentration of the neat CNC layer. For the CPL measurement of R6G@CNC5||CNC*x* films, the light passes the R6G@CNC5 layer first and then the neat CNC layer (Figure 2a). Generally, we compared the g_{lum} factor of different devices in this mode, if without specific notes. Since the chiral nematic CNCs films normally reflect left-handed light but are transparent to right-handed light at the PBG band, the signals obtained in this mode is right-handed light. The four double-layered devices emitted right-handed CPL light, and they showed a significant increase (3−4 times) in their CPL g_{lum} (Figure 2b). The absolute quantum yields of single-layer devices and corresponding double-layer devices were measured and listed in Table S1. The change of device structures has no influence to the quantum yield. The g_{lum} factor increased to −0.936 at 575 nm for R6G@CNC5||CNC5, −0.69 for CV@CNC5||CNC5 at 655 nm, and −0.48 at 675 nm and −0.51 at 510 nm for the MB@CNC5||CNC5 or Si QDs@CNC5||CNC5, respectively. Although the g_{lum} of R6G and CV were similar in their single-layer devices, they showed a big difference in the double-layered devices. We suppose it may relate to the PBG band of the CNC5 for CV. Because to match the PBG band with the emission band of CV, PEG has been added in the CNC layer for the CV device (Figure S6). To confirm it, the g_{lum} values of the CV@PMMA||CNC5 devices were measured (Figure S5b), and it is −0.421 at 650 nm, lower than the −0.74 at 577 nm of R6G@PMMA||CNC5 (Figure S4a).

On the other hand, we compared the g_{lum} factor of the double-layered device R6G@CNC5||CNC5 (−0.936) with the single-layered device R6G@PMMA||CNC5 or R6G (aq)||CNC5. The double-layered device showed a higher CPL dissymmetry factor than these two single-layered devices, indicating both two CNC layers of double-layered devices have contributed to the large g_{lum} factor, but the effect of the neat layer was dominant. By taking off −0.24 (the g_{lum} of R6G@CNC5) from the −0.936 (R6G@CNC5||CNC5), we found that the contribution of the clean CNC5 layer in the double-layered devices was ∼−0.7, approaching the value in the R6G@PMMA||CNC5 and R6G (aq)||CNC5 cases (−0.74). This part of g_{lum} (∼−0.7) can be assigned to the contribution of a clean CNC5 layer. Therefore, when the fluorophores dispersed in a chiral nematic CNCs matrix (g_{lum} of R6G −0.24), the light reflection and the random scattering by the CNC matrix decrease the dissymmetry of light to 1/3. We have repeated the R6G@CNC5||CNC5 in different batches, and all presented similar g_{lum} factors, even after adding a small amount of graphene or carbon black in the R6G@CNCs layer for limiting the background scattering in composite films[47] (Figure S7). The g_{lum} factors in different batches match up very well, showing the robustness of these device structures. In addition, the negative g_{lum} value of R6G@CNC5||CNC5 devices was recorded when the measurement was conducted from the reverse side, showing a right-handed emission light (Figure S8). It is different from the single-layered devices, in which a left-handed light was recorded from the reverse side (Figure S4). A marginal improvement of reverse-side double-layer devices CNC5||R6G@CNC5 presented in g_{lum} factor compared to the single-layer R6G@CNC5 (Figure S8). In addition, "front-side and back-side" and "rotation" measurements of the CD and CPL spectra for R6G@CNC5||CNC5 and MB@CNC5||CNC5 confirmed that there is no linear polarization in the CPL[48] (Figures S9 and S10). The double-layer CPL systems consisting of a CPL layer and a CLC layer have been used in modulating the g_{lum} of CPL,[16] enhancing the g_{lum} factor from 0.25 to 1.43 in liquid crystals,[16] or −0.35 to −1.00 in the CNC solid film.[20] The comparison of single-layered devices (SiQDs@PMMA||CNC5, CV@PMMA||CNC5, MB@PMMA||CNC5) with the corresponding double-layered devices also indicates that the neat CNC layer plays a major role in the g_{lum} value (Figure S5). The detailed analysis of the effects from both CNCs layers may help us find a pathway to optimize device structures.

3.3. Impact of the Pitch Number of the Clean CNC Layer. The thickness of CNCs' chiral nematic layers showed an influence on the g_{lum} factor.[36,49,50] Because the film thickness was related to the concentration of CNC aqueous solution in assembly, we changed it by varying CNC concentration (Table 1). In the study of R6G@CNCs single-layer devices (Figure S3), we observed that the $|g_{lum}|$ gradually increased from 0.237 to 0.292 with a concentration of 3 wt % (35 μm) to 9 wt % (90 μm). How about the tendency of g_{lum} with the concentration of the clean CNCs layer in the double-layered devices? To explore the upper limit of the increase of g_{lum} factor by increasing thickness, we compared the g_{lum} factor in the R6G and MB series, while the thickness of the neat CNCs layer varied (Figures 3 and S11). Surprisingly, the g_{lum} of the R6G series was changed from −0.423 to −1.055 when the concentration used in the clean CNC layer changed from 3 to 7 wt %; then, the value decreased slightly from 8 wt % CNC solution. The g_{lum} factor presented the top (−1.055) at the 7 wt % (Figure 3a). The MB series also showed a top limit in g_{lum} (Figure 3b), corresponding to the thickness of the CNC layer ∼75 μm at 7 wt % CNC systems (Table 1), but the g_{lum} factor was −0.584 only.

Why the R6G series presented better in the CPL dissymmetry, although the film thickness of CNCs showed little change in R6G and MB cases? Both R6G and MB have the narrow Stokes shift (Figure S12), their absorption and emission wavelengths can be covered in the PBG band of CNCs layers to a certain extent (Table S2). We have made our best for matching the emission wavelength of luminophores with the PBG band of CNCs in the two systems (Figure S1). Certainly, R6G has a strong emission and high quantum yield

https://doi.org/10.1021/acsomega.3c02969
ACS Omega 2023, 8, 23191−23201

Table 1. Thickness and Pitch Numbers of the Assembled CNC Layers in R6G and MB Series by Using Different Concentrations of CNC Solutions

the concentration of CNCs (wt %)	sample series	the thickness of the CNCs layer (μm)	numbers of pitch
3	R6G series	35.25 ± 0.05	93
	MB series	36.74 ± 0.12	80
4	R6G series	44.67 ± 0.03	119
	MB series	45.95 ± 0.09	104
5	R6G series	58.52 ± 0.27	158
	MB series	59.68 ± 0.14	136
6	R6G series	61.17 ± 0.15	174
	MB series	63.05 ± 0.08	141
7	R6G series	75.32 ± 0.12	210
	MB series	76.54 ± 0.21	170
8	R6G series	81.13 ± 0.08	220
	MB series	83.62 ± 0.05	184
9	R6G series	90.69 ± 0.09	241
	MB series	93.04 ± 0.07	204

than MB does, which may mainly contribute to its large g_{lum} factor. Is there any other factor possibly contributing to g_{lum}?

We noticed that the pitch number of these clean CNC layers for R6G@CNCs and MB@CNCs was different at the similar film thickness because the PBG band of CNCs layers was modulated to match the emission band of luminophores. In the thickness-fixed CNC films, the pitch number will decrease when the PBG increases. We thought in different luminophores cases the thickness of the CNC film may not represent the twisted strength directly; alternatively, the pitch number can directly reflect how strong the light has been twisted when it passed the chiral field. We considered that using the pitch number to determine the twisted strength of the chiral field was more suitable for CNC systems with different luminophores than the film's thickness. For CNCx (x = 3, 9 wt %) of the clean CNC layer in double-layered devices, the film thickness of 35 or 90 μm in R6G series corresponds to the pitch number 93 or 241, respectively, while the thickness in MB@CNC5||CNCx (x = 3, 9 wt %) series slightly increased to 36 or 93 μm due to the addition of PEG; however, the corresponding pitch number decreased to 80 and 204, respectively (Table 1). The change in pitch number was more significant than that of film thickness, which may partly explain why the increment of $|g_{lum}|$ in the R6G double-layered devices was higher than that of MB double-layered devices (Figure 3e). Similarly, the difference in the g value between R6G and CV double-layered devices was also because of the different pitch numbers in their neat CNC films.

The other question is why the g_{lum} factor cannot be increased further by using a higher concentration of CNC solutions. These CNC films formed by using concentrated CNC solutions presented well-assembled structures as observed in these SEM images (Figure S11a,b), and their PBG bands were located at the same range (Figure S11c,d). To elucidate the assembled structure of CNC films in different concentrations in detail, we have conducted the GI-WAXS measurement for comparing the assembled CNCs structures of different concentrations. The change in the orientation degree and fwhm of these films was not significant (Figure S13). Based on these characterizations, we tentatively excluded a significant influence of CNC-assembled structures. We propose that the increasing light scattering with the increase in thickness of CNCs may offset the twisting effect of the chiral field to the light, leading to the top limit of the $|g_{lum}|$ with the increase in CNC thickness. On the other hand, the length/diameter (L/D) ratio of the CNCs we used in these films was about 4−5, and there were many threads of CNCs which increases the polydispersity index of the CNC system (Figure S14). According to the Onsager's theory[23] and the Frenkel's study,[51−55] an increasing L/D ratio of CNCs will enhance the order of CNC assembled nanostructures, which may strengthen their effect on twisting light.

3.4. Enhancing the Emission Dissymmetry Factor by Adding AuNR@SiO_2. Amplification of the intensity and dissymmetry factors of circularly polarized light is desired to broaden the range of applications of circularly polarized luminescence.[46] Because the radiative emission rate of fluorophores is generally enhanced at the surface of gold nanostructures, especially in the case the surface plasmon resonance frequency of gold covered the emission spectrum of the luminophore; thus, in our study, gold nanorods coated with a thin SiO_2 layer have been utilized in the MB@CNC series to increase their emission intensity. MB, gold nanorods coated with a SiO_2 layer (Au NRs@SiO_2, Figure S15), and CNCs were mixed to make the emission layer. This sample named MAS@CNCx series, where the x represented the concentration of CNC solution. UV−vis spectra showed the location of the plasmon bands of AuNR@SiO_2 (solid curve), PBG band of CNCs (dot-line curve), and photoemission spectrum of MB (dashed curve) (Figure 4a). The absorption and PL spectra of these hybrid systems are shown in Figures S16 and S17. The CPL spectra of these double-layered devices of MAS@CNC5||CNC5 are presented in Figure 4b−d. The effect of the plasmon band of AuNR@SiO_2 on the g_{lum} factor of MAS@CNC5||CNC5 double-layered devices is shown in Figure S18. When the PBG of CNCs, the plasmonic absorption of AuNR@SiO_2 (λ_{LSPR} = 670 nm), and the luminescence band of MB have a good match (Figure 4a), the PL intensity is significantly enhanced (MAS@CNC5) (Figures S17 and 4b). The absolute quantum yield of MAS devices increased from 3.8 to 23.65% in the presence of AuNR@SiO_2 (λ_{LSPR} = 670 nm) (Table S3). Meanwhile, the asymmetry factor of MB photoluminescence was enhanced from −0.584 (MB@CNC5||CNC7) to −0.608 at MAS@CNC5||CNC7 (λ_{LSPR} = 670 nm) (Figures 3d and 4d), and the increment ratio was about 15%. According to literature report, the AuNR@SiO_2 can be aligned inside the CNC film along the direction of CNC rods in each nematic layer.[56,57] The aligned gold nanorods show clearly anisotropic polarized emission properties,[58] which may result in the different enhancement between LCP and RCP.[59] Based on the definition of g_{lum} factor, $g_{lum} = 2 \times (I_L - I_R)/(I_L + I_R)$, the different enhancements of LCP and RCP will lead to the increase of the g_{lum} factor. In the previous study of MB with Au@SiO_2 triangular nanoprisms, a 201-fold enhancement of the MB

https://doi.org/10.1021/acsomega.3c02969
ACS Omega 2023, 8, 23191−23201

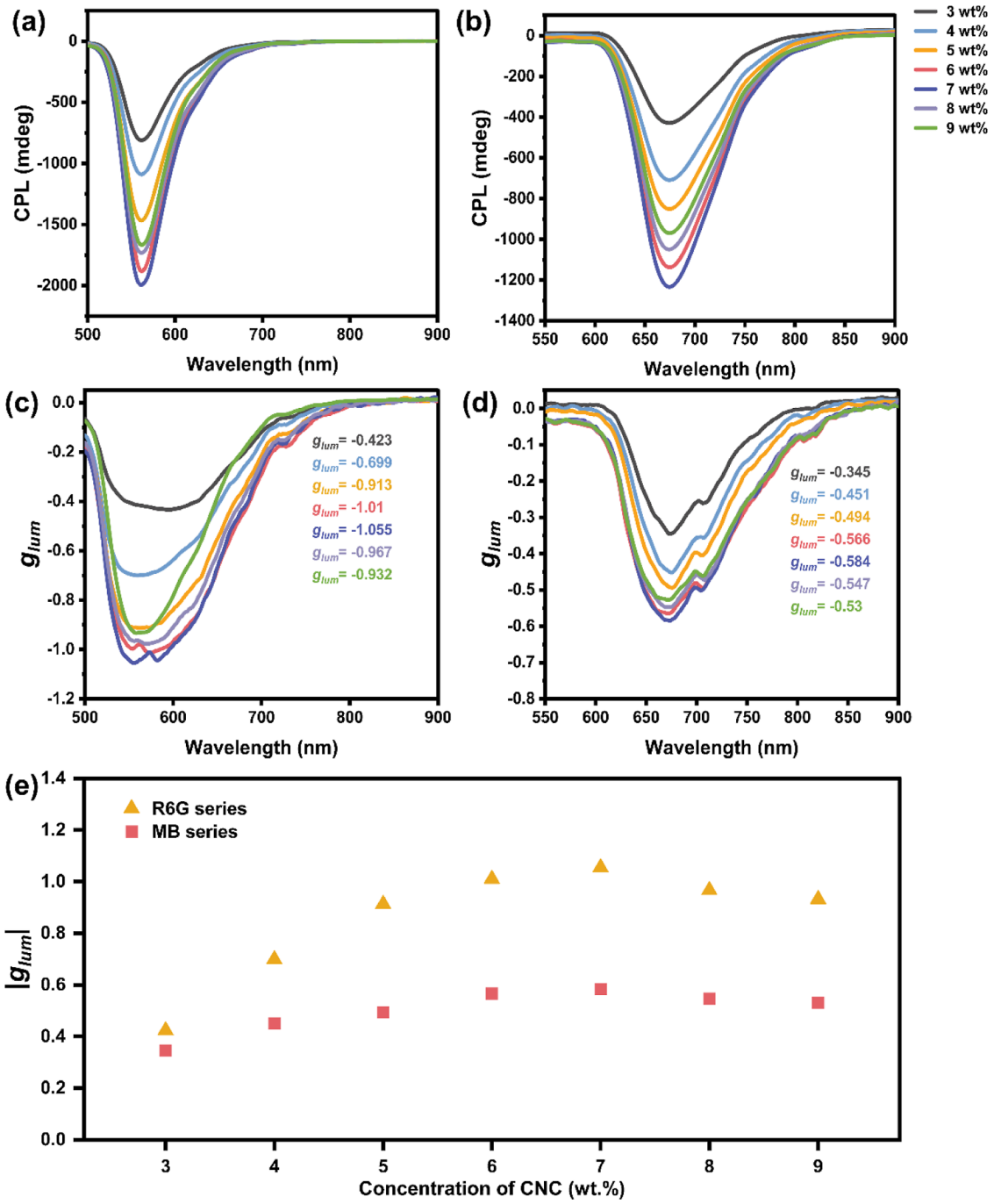

Figure 3. Variation of CPL spectra and g_{lum} factors with the increase in concentration of the clean CNC layer. (a,c) R6G@CNC5||CNC*x* series. (b,d) MB@CNC5||CNC*x* series. *x* = 3, 4, 5, 6, 7, 8, and 9 wt %, respectively. (e) The comparison of the $|g_{lum}|$ of R6G and MB series in the different concentrations of neat CNCs layers from 3 to 9 wt %.

fluorescence intensity has been achieved, and the g factor was changed from −0.055 to −0.085.[46]

4. CONCLUSIONS

In this study, we have investigated the CPL systems based on CNC-assembled nanostructures and achiral luminophores. We compared the CPL performance of four fluorophores, Si QDs, R6G, CV, and MB. Different device structures, such as single-layered devices, in which dye was dispersed in the CNC layer or separated with the CNC layer, and double-layered devices in which dye was dispersed in the CNC layer and a clean CNC layer was added, were explored to discover their impact on the g_{lum} of CPL devices. The double-layered device structure showed a significant effect on enhancing the g_{lum} factor for all four fluorophores, with a 3−4 times enhancement. The thickness of the CNC layer impacts the g_{lum} factors as well, but it showed a monotone increase in single-layered devices, whereas in the double-layered devices, the increase because of the increasing thickness achieved the limit at the 7 wt % CNCs. Because the PBG band of CNC layers for different dyes have been adjusted to match the emission band of dyes, we found that the increase of pitch number in the CNC layer is more directly related to the increase of g_{lum}. R6G showed the best performance in CPL intensity and g_{lum} factor, no matter the

https://doi.org/10.1021/acsomega.3c02969
ACS Omega 2023, 8, 23191−23201

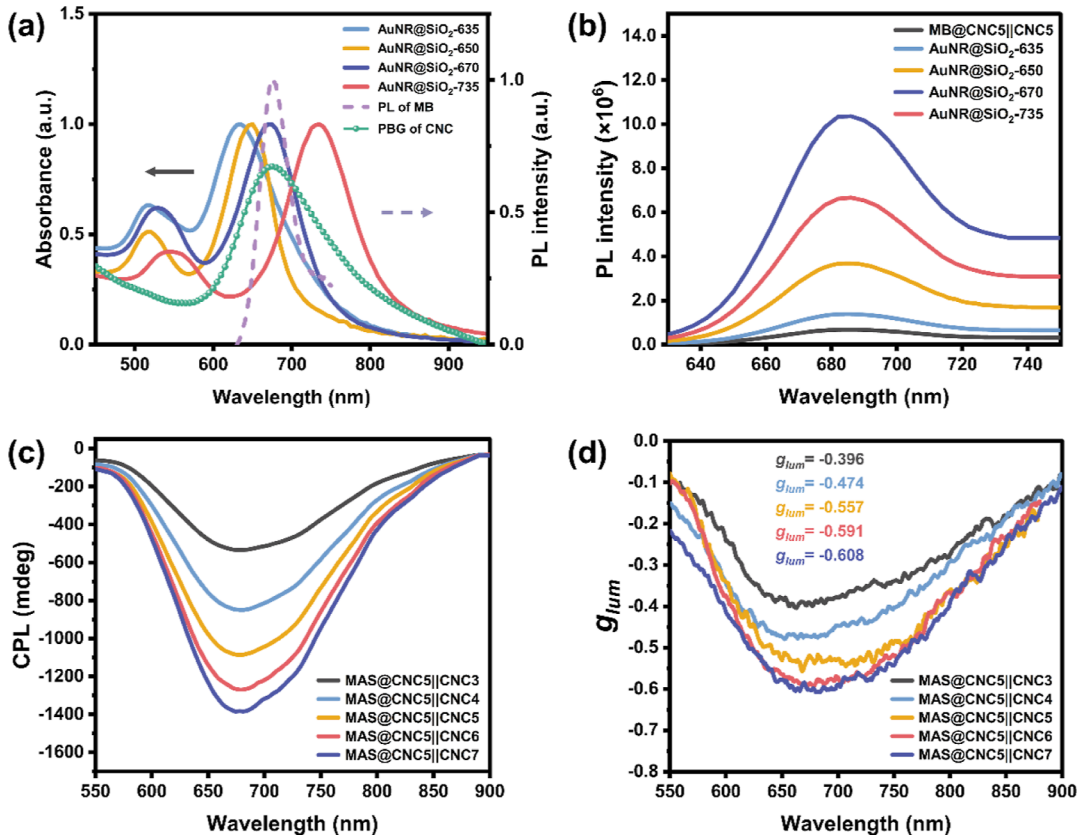

Figure 4. (a) UV−vis absorption spectra of AuNR@SiO_2 with different plasmon bands (solid curve) and PBG band of CNCs (dot-line curve). The location of photoemission spectrum of MB (dashed curve) was shown to find the proper AuNR@SiO_2 sample. (b) Photoluminescence spectra of MAS@CNC5||CNC5 double layer films loaded with AuNR@SiO_2 with different plasmon bands. The AuNR@SiO_2 (λ_{LSPR} = 670 nm) presented the best PL enhancement. The amount of MB added in all devices was kept at 5×10^{-3} mg. (c,d) CPL spectra and corresponding g_{lum} values of MAS@CNC5||CNCx (λ_{LSPR} = 670 nm) with the increase in concentration of the CNC layer, x = 3, 4, 5, 6, and 7 wt %, respectively.

device structure. The g_{lum} factor was −0.258 for R6G@CNC5 and −1.055 at 575 nm for R6G@CNC5||CNC7. Although MB was a weak fluorophore and showed a low g_{lum} factor of −0.153 in MB@CNC5, the g_{lum} factor can be further increased by adding AuNR@SiO_2 with a proper plasmon band, achieving −0.608 at 675 nm in MAS@CNC5||CNC7 (λ_{LSPR} = 670 nm). The study analyzed detailed structural parameters that may influence the dissymmetric factor of the CNC-based right-handed CPL devices. It will benefit the further development of good CPL devices based on the chiral nematic structure of CNCs.

■ ASSOCIATED CONTENT

Supporting Information

The Supporting Information is available free of charge at https://pubs.acs.org/doi/10.1021/acsomega.3c02969.

PL spectra, CD spectra, CPL spectra, matching degree of the emitter layer and the pure CNC layer in the R6G and CV devices, cross-sectional SEM images, absorption spectra, GI-WAXS measurement data, AFM images, UV−vis spectra, absolute quantum yields, and comparison of the excitation and PL wavelength of luminophores with the PBG band of CNC films (PDF)

■ AUTHOR INFORMATION

Corresponding Author

Zhaoxia Jin − *Key Laboratory of Advanced Light Conversion Materials and Biophotonics, Department of Chemistry, Renmin University of China, 100872 Beijing, People's Republic of China;* orcid.org/0000-0002-6108-0636; Email: jinzx@ruc.edu.cn

Authors

Guodan Wei − *Key Laboratory of Advanced Light Conversion Materials and Biophotonics, Department of Chemistry, Renmin University of China, 100872 Beijing, People's Republic of China*

Mengfan Lu − *Key Laboratory of Advanced Light Conversion Materials and Biophotonics, Department of Chemistry, Renmin University of China, 100872 Beijing, People's Republic of China*

Kai Feng − *Key Laboratory of Advanced Light Conversion Materials and Biophotonics, Department of Chemistry, Renmin University of China, 100872 Beijing, People's Republic of China*

Sijia Ma − *Beijing National Laboratory for Molecular Science (BNLMS), Key Laboratory of Colloid, Interface and Chemical Thermodynamics, Institute of Chemistry, Chinese Academy of Sciences, 100190 Beijing, People's Republic of China; Key Laboratory of Nanosystem and Hierarchical Fabrication, National Center for Nano-Science and Technology, 100190 Beijing, People's Republic of China*

https://doi.org/10.1021/acsomega.3c02969
ACS Omega 2023, 8, 23191−23201

Yuqian Jiang − *Key Laboratory of Nanosystem and Hierarchical Fabrication, National Center for Nano-Science and Technology, 100190 Beijing, People's Republic of China;* orcid.org/0000-0002-7013-4704

Complete contact information is available at: https://pubs.acs.org/10.1021/acsomega.3c02969

Notes

The authors declare no competing financial interest.

■ ACKNOWLEDGMENTS

This work was supported by the National Natural Science Foundation of China (grant 51673210 and 21973020). We would like to express our thanks to Prof. J. P. Zhang at Renmin University of China for his useful discussion and suggestion. We are grateful for the GI-WAXS measurement on beamline BSRF-1W1A, BEPC under project number 2022-BEPC-PT-007067. The authors gratefully acknowledge the cooperation of the beamline scientists at the BSRF-1W1A beamline.

■ REFERENCES

(1) Zheng, H.; Li, W.; Li, W.; Wang, X.; Tang, Z.; Zhang, S. X.-A.; Xu, Y. Uncovering the Circular Polarization Potential of Chiral Photonic Cellulose Films for Photonic Applications. *Adv. Mater.* **2018**, *30*, 1705948.

(2) Furumi, S. Recent Progress in Chiral Photonic Band-Gap Liquid Crystals for Laser Applications. *Chem. Rec.* **2010**, *10*, 394−408.

(3) Gong, Z.-L.; Zhu, X.; Zhou, Z.; Zhang, S.-W.; Yang, D.; Zhao, B.; Zhang, Y.-P.; Deng, J.; Cheng, Y.; Zheng, Y.-X.; Zang, S.-Q.; Kuang, H.; Duan, P.; Yuan, M.; Chen, C.-F.; Zhao, Y. S.; Zhong, Y.-W.; Tang, B. Z.; Liu, M. Frontiers in Circularly Polarized Luminescence: Molecular Design, Self-Assembly, Nanomaterials, and Applications. *Sci. China: Chem.* **2021**, *64*, 2060−2104.

(4) Wang, X.; Wang, Q.; Zhang, X.; Miao, J.; Cheng, J.; He, T.; Li, Y.; Tang, Z.; Chen, R. Circularly Polarized Light Source from Self-Assembled Hybrid Nanoarchitecture. *Adv. Opt. Mater.* **2022**, *10*, 2200761.

(5) Han, D. X.; Yang, X. F.; Han, J. L.; Zhou, J.; Jiao, T. F.; Duan, P. F. Sequentially Amplified Circularly Polarized Ultraviolet Luminescence for Enantioselective Photopolymerization. *Nat. Commun.* **2020**, *11*, 5659.

(6) Ben-Moshe, A.; Maoz, B.; Govorov, A. O.; Markovich, G. Chirality and Chiroptical Effects in Inorganic Nanocrystal Systems with Plasmon and Exciton Resonances. *Chem. Soc. Rev.* **2013**, *42*, 7028−7041.

(7) Greenfield, J. L.; Wade, J.; Brandt, J. R.; Shi, X.; Penfold, T. J.; Fuchter, M. J. Pathways to Increase the Dissymmetry in the Interaction of Chiral Light and Chiral Molecules. *Chem. Sci.* **2021**, *12*, 8589−8602.

(8) Sang, Y.; Han, J.; Zhao, T.; Duan, P.; Liu, M. Circularly Polarized Luminescence in Nanoassemblies: Generation, Amplification, and Application. *Adv. Mater.* **2020**, *32*, 1900110.

(9) Huang, S.; Yu, H.; Li, Q. Supramolecular Chirality Transfer toward Chiral Aggregation: Asymmetric Hierarchical Self-Assembly. *Adv. Sci.* **2021**, *8*, 2002132.

(10) Mitov, M.; Dessaud, N. Going Beyond the Reflectance Limit of Cholesteric Liquid Crystals. *Nat. Mater.* **2006**, *5*, 361−364.

(11) Zhang, X.; Xu, Y.; Valenzuela, C.; Zhang, X.; Wang, L.; Feng, W.; Li, Q. Liquid Crystal-Templated Chiral Nanomaterials: From Chiral Plasmonics to Circularly Polarized Luminescence. *Light: Sci. Appl.* **2022**, *11*, 223.

(12) Zhang, M.; Wang, Y.; Zhou, Y.; Yuan, H.; Guo, Q.; Zhuang, T. Amplifying Inorganic Chirality Using Liquid Crystals. *Nanoscale* **2022**, *14*, 592−601.

(13) Li, C.; Yang, X.; Han, J.; Sun, W.; Duan, P. Signal Transmission Encryption Based on Dye-Doped Chiral Liquid Crystals Via Tunable and Efficient Circularly Polarized Luminescence. *Mater. Adv.* **2021**, *2*, 3851−3855.

(14) Chen, S. H.; Katsis, D.; Schmid, A. W.; Mastrangelo, J. C.; Tsutsui, T.; Blanton, T. N. Circularly Polarized Light Generated by Photoexcitation of Luminophores in Glassy Liquid-Crystal Films. *Nature* **1999**, *397*, 506−508.

(15) Yao, K.; Shen, Y.; Li, Y.; Li, X.; Quan, Y.; Cheng, Y. Ultrastrong Red Circularly Polarized Luminescence Promoted from Chiral Transfer and Intermolecular Förster Resonance Energy Transfer in Ternary Chiral Emissive Nematic Liquid Crystals. *J. Phys. Chem. Lett.* **2021**, *12*, 598−603.

(16) Lin, S.; Zeng, S.; Li, Z.; Fan, Q.; Guo, J. Turn-on Mode Circularly Polarized Luminescence in Self-Organized Cholesteric Superstructure for Active Photonic Applications. *ACS Appl. Mater. Interfaces* **2022**, *14*, 30362−30370.

(17) Yan, J.; Ota, F.; San Jose, B. A.; Akagi, K. Chiroptical Resolution and Thermal Switching of Chirality in Conjugated Polymer Luminescence Via Selective Reflection Using a Double-Layered Cell of Chiral Nematic Liquid Crystal. *Adv. Funct. Mater.* **2017**, *27*, 1604529.

(18) Zhao, S.; Yu, Y.; Zhang, B.; Feng, P.; Dang, C.; Li, M.; Zhao, L.; Gao, L. Dual-Mode Circularly Polarized Light Emission and Metal-Enhanced Fluorescence Realized by the Luminophore−Chiral Cellulose Nanocrystal Interfaces. *ACS Appl. Mater. Interfaces* **2021**, *13*, 59132−59141.

(19) Wei, L.; Ma, X.; Xu, Y. A Double Layer Laminated Film of Cellulose Nanocrystals and Dye Displaying Vibrant Circularly Polarized Light. *Chem. Res. Chin. Univ.* **2022**, *38*, 45−49.

(20) Duan, C.; Wang, B.; Li, J.; Xu, J.; Zeng, J.; Li, J.; Zhao, Z.; Gao, W.; Ying, G.; Chen, K. Switchable Circularly Polarized Signals with High Asymmetric Factor Triggered by Dual Photonic Bandgap Structure. *Small* **2022**, *18*, 2204199.

(21) Trache, D.; Hussin, M. H.; Haafiz, M. K. M.; Thakur, V. K. Recent Progress in Cellulose Nanocrystals: Sources and Production. *Nanoscale* **2017**, *9*, 1763−1786.

(22) George, J.; Sabapathi, S. N. Cellulose Nanocrystals: Synthesis, Functional Properties, and Applications. *Nanotechnol., Sci. Appl.* **2015**, *8*, 45−54.

(23) Onsager, L. The Effects of Shape on the Interaction of Colloidal Particles. *Ann. N.Y. Acad. Sci.* **1949**, *51*, 627−659.

(24) Beck-Candanedo, S.; Roman, M.; Gray, D. G. Effect of Reaction Conditions on the Properties and Behavior of Wood Cellulose Nanocrystal Suspensions. *Biomacromolecules* **2005**, *6*, 1048−1054.

(25) Dong, X. M.; Revol, J.-F.; Gray, D. G. Effect of Microcrystallite Preparation Conditions on the Formation of Colloid Crystals of Cellulose. *Cellulose* **1998**, *5*, 19−32.

(26) Klemm, D.; Kramer, F.; Moritz, S.; Lindström, T.; Ankerfors, M.; Gray, D.; Dorris, A. Nanocelluloses: A New Family of Nature-Based Materials. *Angew. Chem., Int. Ed.* **2011**, *50*, 5438−5466.

(27) Mu, X.; Gray, D. G. Formation of Chiral Nematic Films from Cellulose Nanocrystal Suspensions Is a Two-Stage Process. *Langmuir* **2014**, *30*, 9256−9260.

(28) Revol, J. F.; Bradford, H.; Giasson, J.; Marchessault, R. H.; Gray, D. G. Helicoidal Self-Ordering of Cellulose Microfibrils in Aqueous Suspension. *Int. J. Biol. Macromol.* **1992**, *14*, 170−172.

(29) Xu, M.; Li, G.; Li, W.; An, B.; Sun, J.; Chen, Z.; Yu, H.; Li, J.; Yang, G.; Liu, S. Exploring the Circular Polarization Capacity from Chiral Cellulose Nanocrystal Films for a Photo-Controlled Chiral Helix of Supramolecular Polymers. *Angew. Chem., Int. Ed.* **2022**, *61*, No. e202117042.

(30) Li, W.; Xu, M.; Ma, C.; Liu, Y.; Zhou, J.; Chen, Z.; Wang, Y.; Yu, H.; Li, J.; Liu, S. Tunable Upconverted Circularly Polarized Luminescence in Cellulose Nanocrystal Based Chiral Photonic Films. *ACS Appl. Mater. Interfaces* **2019**, *11*, 23512−23519.

(31) Xu, M.; Wu, X.; Yang, Y.; Ma, C.; Li, W.; Yu, H.; Chen, Z.; Li, J.; Zhang, K.; Liu, S. Designing Hybrid Chiral Photonic Films with Circularly Polarized Room-Temperature Phosphorescence. *ACS Nano* **2020**, *14*, 11130−11139.

(32) Kim, M.; Lee, H.; Snipes, R. T.; Han, M. J.; Tsukruk, V. V. Co-Assembly of Biosynthetic Chiral Nematic Adhesive Materials with Dynamic Polarized Luminescence. *Small* **2022**, *18*, 2104340.
(33) Liu, M.; Kuang, K.; Li, G.; Yang, S.; Yuan, Z. Photoluminescence-Enhanced Cholesteric Films: Coassembling Copper Nanoclusters with Cellulose Nanocrystals. *Carbohydr. Polym.* **2021**, *257*, 117641.
(34) Chekini, M.; Prince, E.; Zhao, L.; Mundoor, H.; Smalyukh, I. I.; Kumacheva, E. Chiral Carbon Dots Synthesized on Cellulose Nanocrystals. *Adv. Opt. Mater.* **2020**, *8*, 1901911.
(35) Zhang, T.; Tang, C.; Wang, Y.; Wang, C.; Zhang, Y.; Qi, W.; Su, R.; He, Z. Circularly Polarized Luminescent Chiral Photonic Films Based on the Coassembly of Cellulose Nanocrystals and Gold Nanoclusters. *Langmuir* **2022**, *38*, 4147−4155.
(36) Xu, M.; Ma, C.; Zhou, J.; Liu, Y.; Wu, X.; Luo, S.; Li, W.; Yu, H.; Wang, Y.; Chen, Z.; Li, J.; Liu, S. Assembling Semiconductor Quantum Dots in Hierarchical Photonic Cellulose Nanocrystal Films: Circularly Polarized Luminescent Nanomaterials as Optical Coding Labels. *J. Mater. Chem. C* **2019**, *7*, 13794−13802.
(37) Refractive index database. Optical Constants of Schott - Bk (Borosilicate Crown). https://refractiveindex.info/?shelf=glass&book=SCHOTT-BK&page=BK7G18 (Retrieved April 28, 2023).
(38) Feng, K.; Wei, G.; Lu, M.; Gao, N.; Wang, Y.; Jin, Z. Optimizing the Performance of the near-Infrared (Nir) Photothermal Conversion Via Modulating the Domain Size of the Chiral Nematic Phase in Co-Assembled Cellulose Nanocrystal Composite Films. *J. Mater. Chem. C* **2022**, *10*, 13183−13190.
(39) Feng, K.; Lu, M.; Wei, G.; Tang, F.; Jin, Z. Cellulose Nanocrystals/Poly(3,4-Ethylenedioxythiophene) Photonic Crystal Composites with Electrochromic Properties for Smart Windows, Displays, and Anticounterfeiting/Encryption Applications. *ACS Appl. Nano Mater.* **2022**, *5*, 10848−10859.
(40) Nikoobakht, B.; El-Sayed, M. A. Preparation and Growth Mechanism of Gold Nanorods (Nrs) Using Seed-Mediated Growth Method. *Chem. Mater.* **2003**, *15*, 1957−1962.
(41) Zhang, C.; Yan, Z.-P.; Dong, X.-Y.; Han, Z.; Li, S.; Fu, T.; Zhu, Y.-Y.; Zheng, Y.-X.; Niu, Y.-Y.; Zang, S.-Q. Enantiomeric Mof Crystals Using Helical Channels as Palettes with Bright White Circularly Polarized Luminescence. *Adv. Mater.* **2020**, *32*, 2002914.
(42) Huang, J.-C.; Ye, G.-M.; Yu, M.; Huang, R.; Zhao, Z.; Qin, A.; Wu, S.-T.; Xie, Z. Circularly Polarized Luminescence of Achiral Metal−Organic Colloids and Guest Molecules in a Vortex Field. *Chem.—Eur. J.* **2021**, *27*, 6760−6766.
(43) Li, Q.; Lu, X.; Lv, Z.; Zhu, B.; Lu, Q. Full-Color and Switchable Circularly Polarized Light from a Macroscopic Chiral Dendritic Film through a Solid-State Supramolecular Assembly. *ACS Nano* **2022**, *16*, 18863−18872.
(44) Li, P.; Gao, X.; Zhao, B.; Pan, K.; Deng, J. Multi-Color Tunable and White Circularly Polarized Luminescent Composite Nanofibers Electrospun from Chiral Helical Polymer. *Adv. Fiber Mater.* **2022**, *4*, 1632−1644.
(45) Lee, S.; Lim, Y.-C.; Kim, H.; Seo, D. H.; Na, J.; Kim, H.; Nam, K. T.; Jeong, Y. Random Lasing with a High Degree of Circular Dichroism by Chiral Plasmonic Gold Nanoparticles. *ACS Photonics* **2022**, *9*, 613−620.
(46) Zhao, S.; Yu, Y.; Zhang, B.; Feng, P.; Dang, C.; Li, M.; Zhao, L.; Gao, L. Metal-Enhanced Circularly Polarized Luminescence of Self-Assembled Au@SiO_2 Triangular Nanoprisms and Fluorophores in Chiral Cellulose Nanocrystal Films. *Adv. Opt. Mater.* **2021**, *9*, 2100907.
(47) Zeng, M.; King, D.; Huang, D.; Do, C.; Wang, L.; Chen, M.; Lei, S.; Lin, P.; Chen, Y.; Cheng, Z. Iridescence in Nematics: Photonic Liquid Crystals of Nanoplates in Absence of Long-Range Periodicity. *Proc. Natl. Acad. Sci. U.S.A.* **2019**, *116*, 18322−18327.
(48) Chu, G.; Yin, H.; Jiang, H.; Qu, D.; Shi, Y.; Ding, D.; Xu, Y. Ultrafast Optical Modulation of Rationally Engineered Photonic−Plasmonic Coupling in Self-Assembled Nanocrystalline Cellulose/Silver Hybrid Material. *J. Phys. Chem. C* **2016**, *120*, 27541−27547.
(49) Shi, H.; Conger, B. M.; Katsis, D.; Chen, S. H. Circularly Polarized Fluorescence from Chiral Nematic Liquid Crystalline Films: Theory and Experiment. *Liq. Cryst.* **1998**, *24*, 163−172.
(50) Wan, L.; Wade, J.; Salerno, F.; Arteaga, O.; Laidlaw, B.; Wang, X.; Penfold, T.; Fuchter, M. J.; Campbell, A. J. Inverting the Handedness of Circularly Polarized Luminescence from Light-Emitting Polymers Using Film Thickness. *ACS Nano* **2019**, *13*, 8099−8105.
(51) Stroobants, A.; Lekkerkerker, H. N. W.; Frenkel, D. Evidence for One-Two-and Three-Dimensional Order in a System of Hard Parallel Spherocylinders. *Phys. Rev. A: At., Mol., Opt. Phys.* **1987**, *36*, 2929−2945.
(52) Frenkel, D.; Lekkerkerker, H. N. W.; Stroobants, A. Thermodynamic Stability of a Smectic Phase in a System of Hard Rods. *Nature* **1988**, *332*, 822−823.
(53) Frenkel, D.; Mulder, B. M.; McTague, J. P. Phase Diagram of a System of Hard Ellipsoids. *Phys. Rev. Lett.* **1984**, *52*, 287−290.
(54) Bates, M. A.; Frenkel, D. Influence of Polydispersity on the Phase Behavior of Colloidal Liquid Crystals: A Monte Carlo Simulation Study. *J. Chem. Phys.* **1998**, *109*, 6193−6199.
(55) Bolhuis, P.; Frenkel, D. Tracing the Phase Boundaries of Hard Spherocylinders. *J. Chem. Phys.* **1997**, *106*, 666−687.
(56) Querejeta-Fernández, A.; Chauve, G.; Methot, M.; Bouchard, J.; Kumacheva, E. Chiral Plasmonic Films Formed by Gold Nanorods and Cellulose Nanocrystals. *J. Am. Chem. Soc.* **2014**, *136*, 4788−4793.
(57) Querejeta-Fernández, A.; Kopera, B.; Prado, K. S.; Klinkova, A.; Methot, M.; Chauve, G.; Bouchard, J.; Helmy, A. S.; Kumacheva, E. Circular Dichroism of Chiral Nematic Films of Cellulose Nanocrystals Loaded with Plasmonic Nanoparticles. *ACS Nano* **2015**, *9*, 10377−10385.
(58) Liu, S.; Li, J.; Li, Z.-Y. Macroscopic Polarized Emission from Aligned Hybrid Gold Nanorods Embedded in a Polyvinyl Alcohol Film. *Adv. Opt. Mater.* **2013**, *1*, 227−231.
(59) Zhao, S.; Zhu, H.; Lu, J.; Li, M.; Zhao, L.; Zhou, L.; Gao, L. Uncovering the Origin of Chirality from Plasmonic Nanoparticle/Cellulose Nanocrystal Composite Films. *Adv. Funct. Mater.* **2022**, *32*, 2201927.

https://doi.org/10.1021/acsomega.3c02969
ACS Omega 2023, 8, 23191−23201